Numerical simulations for the time-averaged acoustic forces acting on rigid cylinders in ideal and viscous fluids



2009 J. Phys. A: Math. Theor. 42 285502

(http://iopscience.iop.org/1751-8121/42/28/285502)

IOP PUBLISHING JOURNAL OF PHYSICS A: MATHEMATICAL AND THEORETICAL

J. Phys. A: Math. Theor. **42** (2009) 285502 (17pp) doi:10.1088/1751-8113/42/28/285502

# Numerical simulations for the time-averaged acoustic forces acting on rigid cylinders in ideal and viscous fluids

**Jingtao Wang and Jurg Dual**

Center of Mechanics, Department of Mechanical and Process Engineering, ETH Zurich, 8092 Zurich, Switzerland

Received 18 November 2008, in final form 29 April 2009
Published 24 June 2009
Online at stacks.iop.org/JPhysA/42/285502

**Abstract**

The time-averaged acoustic forces acting on cylinders in a standing sound field are investigated in detail by finite volume method (FVM) numerical simulations. The forces on a cylinder in an inviscid and a viscous fluid are predicted, and the effects of viscosity are discussed. Furthermore, the secondary forces between two cylinders are also calculated. The numerical results are compared with the theoretical solutions, COMSOL software and the lattice Boltzmann (LB) method, and good agreement is achieved in most cases.

PACS numbers: 02.60.Cb, 47.35.Rs

## 1. Introduction

As is known, an ultrasonic sound field will exert time-averaged forces on particles suspended in a fluid. These forces arise from the transfer of the momentum flux and are a second-order effect of the governing equations [1]. In an ideal fluid, the total time-averaged force exerted on a particle is the acoustic radiation force. It is more complicated in a viscous fluid, because some nonlinear phenomena such as acoustic streaming appear, which influence the momentum transfer between the acoustic field and the particles. Therefore Danilov [2] suggested distinguishing between the radiation force and the mean force which actually act on an object in a viscous fluid.

The time-averaged force can be applied to many practical fields such as acoustic sensors, ultrasonic levitation and contactless particle manipulation [3–5] which has become a hot research topic in ultrasonic devices.

There are a number of theoretical works on the acoustic forces acting on particles. King [6] first calculated the acoustic radiation pressure on rigid sphere particles in an inviscid fluid exerted by planar traveling and standing waves. Then, Yosioka and Kawasima [7] extended King's theory to compressible spheres, and Hasegawa and Yosioka [8] to elastic particles. Gor'kov [9] proposed another more general and simple formulation where the scattered wave

  

potential was determined by the solution for a potential incompressible flow past the sphere. Westervelt [10, 11] took into account the viscosity of the host fluid and the effects of the boundary layer. He calculated the total mean forces from the time-averaged integral of the momentum flux over an arbitrary surface surrounding the particle, which was a quadratic approximation. Doinikov [12] also used this approximation to establish a general solution for a viscous and heat-conducting fluid. This solution can be applied to any symmetric acoustic field without the restriction that the particle radius is much less than the wavelength. Danilov and Mironov [2] also calculated the mean force on a small sphere in a viscous fluid. They also distinguished between the total mean force and the acoustic radiation force. These two forces are equal to each other in an ideal fluid but may differ very much in a viscous fluid due to the effects of the viscous boundary layer surrounding the particle. Recently, Mitri and Fellah [13] deduced new expressions for the radiation force acting on a sphere from the far-field scattering wave field. Although, this approach has a simpler mathematical form, it is difficult to apply it to the viscous cases because of the momentum absorption in the boundary layer. In those cases, the traditional approaches based on the near-field scattering solutions are necessary.

There have also been a few publications for the acoustic radiation forces on cylinders. Awatani [14] gave the first calculation of the acoustic radiation forces acting on a rigid cylinder, and Hasegawa *et al* [15] derived another acoustic radiation function for an elastic cylinder. Their calculations are all with an inviscid fluid and a planar traveling wave. In 1990, Wu and Du [16] reported an analytical solution for a rigid cylinder in an inviscid fluid subjected to a standing wave field. They got a good agreement within 20% errors compared with their experiments. Haydock [17] followed King's [6] original approach and formulated analytical solutions for the radiation force on a fixed or moving rigid cylinder in an ideal fluid due to a standing wave. The solution is approximate, but it is easy to evaluate by using common numerical software packages such as MATLAB. Wei *et al* [18] obtained the analytical formulations for compressible cylinders in a non-viscous fluid in a standing wave field by using the far-field acoustic scattering solution. Mitri and Chen [19] extended the far-field method to gain the theoretical solutions for elastic and viscoelastic cylinders.

In the above papers, the force acting on one particle, namely the primary force, was considered. If two objects are close together in an acoustic field in a fluid, there exist other kinds of forces which are called the secondary forces on each object in addition to the primary force. Many authors (e.g. [20]) investigated these forces with the conditions that the wavelength is much larger than the sphere radius and the spacing between the objects. Under this restriction on the wavelength, Weiser [21] gave the mutual forces between two rigid and compressible particles. Zheng and Apfel [22] calculated the forces between two spheres in a plane wave field under more general conditions without the restriction of the particle spacing.

Numerical work has appeared in recent years and is not as rich as the theoretical works. Townsend *et al* [23] used the computational fluid dynamics (CFD) software and Gor'kov's theory to model the particle paths in a fluid in an ultrasonic standing wave. Their simulations are suited to describing the devices, but did not really investigate the time-averaged forces on particles in detail. By using the lattice Boltzmann (LB) method for solving the Navier–Stokes (N–S) equations in the host medium, Cosgrove *et al* [24] simulated the particle motion in an ultrasound field and compared the results with Wu's [16] theoretical predictions. Haydock [25] also adopted the LB method to calculate the time-averaged forces on a cylinder in a standing wave and compared them with his analytical solutions [17]. However, it should be noted that their simulations both show significant deviations from the theoretical predictions. The reasons may be the restrictions of the LB method and the boundary conditions, which will be discussed later in this paper.

It is necessary to accurately predict the mean forces on suspended particles including the primary force and the secondary force to design ultrasonic particle manipulators. Although there have been many analytical solutions on this topic, it has not been possible to determine the acoustic forces on particles in more complex system conditions such as proximity to the chamber wall, complex viscous function, acoustic streaming and complicated shape of the particle. Therefore, numerical modeling may become a powerful tool. Simple cases can certainly be modeled by commercial software packages such as COMSOL. However, there are some limitations of these software packages in solving more complex problems: it is difficult to apply complicated boundary conditions such as non-reflecting conditions in order to compare the results with theoretical solutions. Also the computational efficiency is not enough for detailed simulations. Consequently, a special numerical method has to be established for calculating the time-averaged acoustic forces acting on particles for the design of ultrasonic particle manipulators. In this paper, we first give an analytical solution for the time-averaged force acting on a rigid cylinder in an inviscid fluid in a standing wave, which is more accurate than the solution in [17], and then efforts are made to calculate the time-averaged forces on one or two rigid cylinders in ideal and viscous fluids subjected to a standing sound wave field by solving the N–S equations directly with the [26, 27] finite volume method (FVM) technique. The numerical results are compared with our theoretical prediction and Haydock's LB simulations [25]. The viscous effects of the host medium and the secondary forces between particles are also investigated in detail.

## 2. Theoretical analysis

Here, a simple analytical solution is presented for the time-averaged force acting on a rigid cylinder in an infinite inviscid fluid in a planar standing wave. The fluid pressure surrounding a fixed particle is given by King [6] as

$$p - p_0 = \rho_0 \dot{\varphi} + \frac{\rho_0}{2c_0^2}\dot{\varphi}^2 - \frac{1}{2}\rho_0 q^2, \tag{1}$$

where $q^2 = \mathbf{u}\cdot\mathbf{u}$, $\mathbf{u} = -\nabla\varphi$ is the velocity vector of the fluid, $\varphi$ is the velocity potential, $\rho_0$ is the density of the undisturbed state, $p_0$ and $p$ are the fluid pressure of the undisturbed state and disturbed state, respectively, and $c_0$ the sound velocity of the fluid. In the cylindrical co-ordinates with the origin at the center of the cylinder as demonstrated in figure 1, where the incident wave is in the $x$-direction, the time-averaged force on the surface of the cylinder in the $x$-direction is

$$F = -\int \langle p\rangle \mathbf{n}\mathrm{d}S = -\frac{a\rho_0}{2c_0^2}\int_0^{2\pi}\langle\dot{\varphi}^2\rangle\cos\theta\mathrm{d}\theta + \frac{a\rho_0}{2}\int_0^{2\pi}\langle q^2\rangle\cos\theta\mathrm{d}\theta = P_\varphi + P_q, \tag{2}$$

where $a$ is the cylinder radius, $P_\varphi$ and $P_q$ are the contributions due to the potential energy and the kinetic energy of the sound wave, respectively.

The total velocity potential is composed of the incident part $\varphi_I$ and the scattered part $\varphi_S$:

$$\varphi = \varphi_T \mathrm{e}^{-\mathrm{i}\omega t} = (\varphi_I + \varphi_S)\mathrm{e}^{-\mathrm{i}\omega t}. \tag{3}$$

The time-independent incident and scattered velocity potential fields are expressed by

$$\varphi_I = A\cos(kr\cos\theta + kh) = \sum_{m=-\infty}^{+\infty} C_m J_m(kr)\mathrm{e}^{\mathrm{i}m\theta}, \tag{4}$$

$$\varphi_S = \sum_{m=-\infty}^{+\infty} B_m H_m^{(1)}(kr)\mathrm{e}^{\mathrm{i}m\theta}. \tag{5}$$

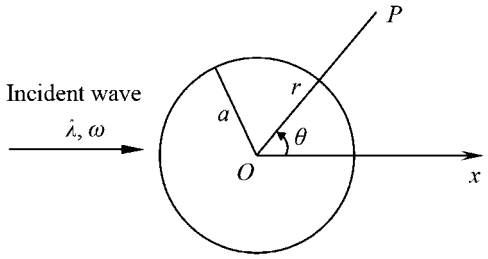


**Figure 1.** The geometry of a cylinder in a standing wave.

Here $h$ is the distance from the nearest velocity node to the center of the cylinder in the $x$-direction, $A$ is the complex amplitude of the velocity potential, $k = \frac{\omega}{c}$ is the wave number, $C_m = \frac{A}{2}[\mathrm{i}^m \mathrm{e}^{\mathrm{i}kh} + (-\mathrm{i})^m \mathrm{e}^{-\mathrm{i}kh}]$ are constants, $J_m(kr)$ and $H_m^{(1)}$ are the $m$th-order Bessel and Hankel function of the first kind, respectively, and $B_m$ are constants defined from the boundary conditions.

The boundary condition on the rigid cylinder surface, $v_r = -\frac{\partial \varphi}{\partial r} = 0$ at $r = a$, yields

$$B_m = -\frac{J_{m-1}(ka) - J_{m+1}(ka)}{H_{m-1}^{(1)}(ka) - H_{m+1}^{(1)}(ka)} C_m. \tag{6}$$

With the constants $B_m$ and the orthogonal relations of trigonometric functions, we have

$$P_\varphi = -\frac{a\rho_0}{2c_0^2}\int_0^{2\pi} \langle \dot{\varphi}^2 \rangle \cos\theta \mathrm{d}\theta = -\frac{a\rho_0\omega^2}{4c_0^2}\mathrm{Re}[\varphi_T \varphi_T^*] = -\frac{\pi a\rho_0\omega^2}{4c_0^2}(I_1^+ + I_1^-), \tag{7}$$

where

$$I_1^\pm = \sum_{m=-\infty}^{+\infty} B_m B_{m\pm1}^* H_m^{(1)} H_{m\pm1}^{(2)} + B_m C_{m\pm1}^* H_m^{(1)} J_{m\pm1} + C_m B_{m\pm1}^* J_m H_{m\pm1}^{(2)} + C_m C_{m\pm1}^* J_m J_{m\pm1}, \tag{8}$$

and

$$P_q = \frac{a\rho_0}{2}\int_0^{2\pi} \langle q^2 \rangle \cos\theta \mathrm{d}\theta = \frac{a\rho_0}{4}\mathrm{Re}\left[\left(\frac{\partial \varphi_T}{a\partial\theta}\right)\left(\frac{\partial \varphi_T}{a\partial\theta}\right)^*\right] = \frac{\pi\rho_0}{4a}(I_2^+ + I_2^-), \tag{9}$$

where

$$I_2^\pm = \sum_{m=-\infty}^{+\infty} m(m\pm1)[B_m B_{m\pm1}^* H_m^{(1)} H_{m\pm1}^{(2)} + B_m C_{m\pm1}^* H_m^{(1)} J_{m\pm1} + C_m B_{m\pm1}^* J_m H_{m\pm1}^{(2)} + C_m C_{m\pm1}^* J_m J_{m\pm1}]. \tag{10}$$

Here, the symbol $*$ means 'the conjugated value of', Re means 'the real part of' and $J_m = J_m(ka)$, $H_m^{(1)} = H_m^{(1)}(ka)$ and $H_m^{(2)} = H_m^{(2)}(ka)$ are the value of the $m$th-order Bessel function and Hankel function of the first and the second kind at $ka$, respectively. Therefore, the total force can be expressed as

$$F = -\frac{\pi a\rho_0}{4}\mathrm{Re}\left[\frac{\omega^2}{c_0^2}(I_1^+ + I_1^-) - \frac{1}{a^2}(I_2^+ + I_2^-)\right]. \tag{11}$$

Note that the final expression (11) for the time-averaged force is an infinite series and is also valid for values of $ka$ larger than $ka \ll 1$. This formula can be conveniently truncated and computed by mathematical software packages such as Mathematica and MATLAB. If small

cylinders are considered which means $ka \ll 1$, it appears sufficient that the terms of $|m| \leqslant 2$ are taken.

We take the same example as in [17], where the fluid is air ($c = 340\,\mathrm{m\,s^{-1}}$, $\rho_0 = 1.2\,\mathrm{kg\,m^{-3}}$) and a 1.4 $\mu$m radius cylinder is located in a standing wave with $\lambda = 0.143$ mm, $A = 3.4\,\mathrm{m\,s^{-1}}$ and $h = 3\lambda/8$. The important value $ka = 0.0615$ in this case. Equation (11) gives the force, $F = -2.813\,76 \times 10^{-6}$ N, with terms up to $|m| \leqslant 2$, $F = -2.813\,31 \times 10^{-6}$ N for both $|m| \leqslant 4$ and $|m| \leqslant 10$. The example shows that it is really enough to take only $|m| \leqslant 2$ terms under the condition $ka \ll 1$. Haydock's [17] solution obtained $F = -2.946 \times 10^{-6}$ N which is quite close to our results. The difference may come from the assumption of Haydock's solution that $h$ must be a small value (less than $0.335\lambda$) and $h = 3\lambda/8$ in this case is not small enough.

The present solution is more common and accurate than Haydock's which only took up to the second-order terms. Moreover, it does not need the condition that $h \leqslant 0.335\lambda$. Furthermore, with some truncations, the computation is not more complicated than Haydock's by using mathematical software packages.

## 3. The governing equations for numerical simulations

The analytical formula (11) is convenient to calculate the time-averaged force on a rigid cylinder in a standing acoustic wave in infinite space, but it is difficult to apply to practical models with complicated boundary conditions and fluid viscosity. Here, we use the fundamental governing equations to calculate the acoustic forces numerically instead of equation (1). The governing equations for a viscous fluid without heat conduction are the N–S equations, which can be expressed as [12]

$$\begin{aligned} &\frac{\partial \rho}{\partial t} + \frac{\partial \rho u_i}{\partial x_i} = 0 \\ &\frac{\partial \rho u_i}{\partial t} + \frac{\partial (\rho u_i u_j + \sigma_{ij})}{\partial x_j} = 0, \end{aligned} \tag{12}$$

where $\sigma_{ij} = p\delta_{ij} - [\eta(\frac{\partial u_i}{\partial x_j} + \frac{\partial u_j}{\partial x_i} - \frac{2}{3}\frac{\partial u_k}{\partial x_k}\delta_{ij}) + \xi\frac{\partial u_k}{\partial x_k}\delta_{ij}]$, $\rho$ is the fluid density, $u_i$ is the fluid velocity, $p$ is the fluid pressure, $\eta$ is the shear viscosity, $\xi$ is the bulk viscosity, and summation over repeated indices is implied as usual. Because the wave amplitude of the acoustic field is small enough in all of the simulations, we use the linear equation of state here:

$$p = p_0 + c_0^2(\rho - \rho_0), \tag{13}$$

where $\rho_0$ and $p_0$ are the density and the fluid pressure of the undisturbed state, respectively, $c_0$ is the sound velocity of the fluid. If we have solved the N–S equations (12) correctly by a numerical method, the results include all of the effects taking place in the fluid such as the acoustic radiation force on an object and acoustic streaming.

The time-averaged forces exerted on a fixed rigid particle in an acoustic field can be calculated by [6, 12]

$$F_i = \left\langle \int_{S_0} -\sigma_{ij} n_j \mathrm{d}S_0 \right\rangle, \tag{14}$$

where the angular bracket means average over one or several periods of the sound wave, $S_0$ is the boundary surface of the particle, and $n_j$ is the $j$th component of the outward unit normal vector of the particle surface. For the inviscid fluid, equation (14) can be simplified as equation (2).

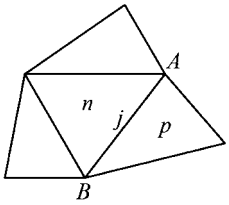


**Figure 2.** Elements and sides.

## 4. Numerical algorithms

The numerical method which we adopt to solve the governing equations (12) is the FVM with the Jameson difference scheme based on triangular meshes. This method, which has second-order accuracy in space, was originally proposed by Jameson [27] in 1981 and then extended to triangular meshes in 1985 [26]. The fourth-order Runge–Kutta method was selected for the time marching, which can improve accuracy and extend the stability region [27]. An advantage of the FVM on triangular meshes is that it can deal with complicated geometrical boundaries conveniently without loss of numerical precision.

Equation (12) can be expressed in the integral form as

$$\frac{1}{\partial t}\int_V \mathbf{U}\mathrm{d}V + \oint_{\partial V} \mathbf{F}\cdot\mathbf{n}\mathrm{d}S = 0, \tag{15}$$

where $\mathbf{U}$ is the vector of conservation parameters, $\mathbf{F}$ is the vector flux matrix which is a function of $\mathbf{U}$, $\partial V$ is the boundary of a certain computational region, and $\mathbf{n}$ is the outward unit normal of $\partial V$. From equation (12), $\mathbf{U}$ and $\mathbf{F}$ are written in Cartesian coordinates as

$$\mathbf{U} = \begin{pmatrix} \rho \\ \rho u_x \\ \rho u_y \\ \rho u_z \end{pmatrix} \text{ and } \mathbf{F} = \begin{pmatrix} \rho u_x\mathbf{i} + \rho u_y\mathbf{j} + \rho u_z\mathbf{k} \\ \left(\rho u_x^2 + \sigma_{xx}\right)\mathbf{i} + (\rho u_x u_y + \sigma_{xy})\mathbf{j} + (\rho u_x u_z + \sigma_{xz})\mathbf{k} \\ (\rho u_x u_y + \sigma_{yx})\mathbf{i} + \left(\rho u_y^2 + \sigma_{yy}\right)\mathbf{j} + (\rho u_y u_z + \sigma_{yz})\mathbf{k} \\ (\rho u_x u_z + \sigma_{zx})\mathbf{i} + (\rho u_y u_z + \sigma_{zy})\mathbf{j} + \left(\rho u_z^2 + \sigma_{zz}\right)\mathbf{k} \end{pmatrix}, \tag{16}$$

where $\mathbf{i}$, $\mathbf{j}$ and $\mathbf{k}$ are the unit vectors in $x$-, $y$- and $z$-directions, respectively, and $\rho$, $u_i$ and $\sigma_{ij}$ are the same as defined in equation (12).

Assuming the conservation equations, equation (15), are satisfied in every triangular element, we obtain the following semi-discrete equations for element $n$ (see figure 2):

$$\frac{\mathrm{d}\mathbf{U}_n}{\mathrm{d}t} = -\frac{1}{\Delta V_n}\sum_{j=1}^{3}\mathbf{F}(\mathbf{U})_{n,j}\cdot\mathbf{n}_j S_j, \tag{17}$$

where $\Delta V_n$ is the volume of the element, $S_j$ is the area of the element side $j$, $\mathbf{F}(\mathbf{U})_{n,j}$ is the flux vector on the side $j$, and $\mathbf{n}_j$ is the outward unit normal vector of the side $j$. The variables on an element surface are computed from the average between its neighbor elements. For instance, the variables flowing through side $j$ between elements $n$ and $p$ which are clear in figure 2 are determined by

$$\mathbf{U}_{n,j} = \frac{\mathbf{U}_n + \mathbf{U}_p}{2}. \tag{18}$$

The Jameson scheme needs artificial dissipative terms to capture shock waves and suppress numerical oscillations. The dissipative terms suggested by Jameson [26, 27] are adopted in our

calculations. The total dissipative term in element $n$ consists of the second- and fourth-order terms:

$$D_n = \sum_{j=1}^{3} d_j^{(2)} + \sum_{j=1}^{3} d_j^{(4)}, \tag{19}$$

where $D_n$ is the total dissipative term of element $n$, and $d_j^{(2)}$ and $d_j^{(4)}$ are the second- and the fourth-order dissipative flux on side $j$, respectively, which can be expressed as (see figure 2)

$$\begin{aligned} d_j^{(2)} &= \varepsilon_j^{(2)}(\mathbf{U}_p - \mathbf{U}_n)_j \\ d_j^{(4)} &= -\varepsilon_j^{(4)}(\nabla^2\mathbf{U}_p - \nabla^2\mathbf{U}_n)_j. \end{aligned} \tag{20}$$

Here the operator $\nabla^2$ means $\nabla^2\mathbf{U}_n = \sum_{p=1}^{3}(\mathbf{U}_p - \mathbf{U}_n)$, and $\varepsilon_j^{(2)}$ and $\varepsilon_j^{(4)}$ are the adapted coefficients for the second- and fourth-order dissipative terms, respectively.

The fourth-order Runge–Kutta method proposed by Deese and Agarwal [28] is used to discretize the time derivative on the left in equation (17). Rewrite equation (17) as

$$\frac{\mathrm{d}\mathbf{U}_n}{\mathrm{d}t} = \mathbf{R}_n(\mathbf{U}_n), \tag{21}$$

where $\mathbf{R}_n(\mathbf{U}_n)$ denotes the right-hand terms of equation (17). Then, the fourth-order Runge–Kutta method can be expressed as

$$\begin{aligned} \mathbf{U}^{(0)} &= \mathbf{U}^m, \\ \mathbf{U}^{(k)} &= \mathbf{U}^{(0)} + \alpha_k \Delta t \mathbf{R}^{(k-1)} \quad , \\ \mathbf{U}^{m+1} &= \mathbf{U}^{(4)}, \end{aligned} \tag{22}$$

where $m$ denotes the last time step and $m+1$ denotes the current time step, $k$ is the Runge–Kutta step number which varies from 1 to 4, $\Delta t$ is the time step, and $\alpha_1 = 1/4$, $\alpha_2 = 1/3$, $\alpha_3 = 1/2$ and $\alpha_4 = 1$, respectively.

Because all of the analytical solutions such as [6, 9, 12, 17] only take the incident and scattered waves on the particle into account without considering waves reflected from boundaries, to compare the numerical results with the analytical predictions, we need non-reflecting boundary conditions. The perfectly matched layer (PML) scheme is one of the popular artificial non-reflecting boundary conditions. The key idea of the PML is to add an extra region (PML) outside the original computational region, into which the outgoing waves are allowed to propagate without any reflections and then dissipated entirely. In our simulations, we adopt a new series of PML formulations for the nonlinear Euler and N–S equations recently proposed by Hu *et al* [29].

## 5. Numerical results and discussions

### *5.1. Computational models*

The time-averaged acoustic force on a fixed cylinder is investigated. The geometrical models and meshes are shown in figure 3. Figure 3(*a*) is the model for investigating the primary force on one cylinder without the PML, and figure 3(*b*) is a typical unstructured triangular mesh used in computation where $R = 80$, $L_x = 1000$ and $L_y = 500$. Figures 3(*c*) and (*d*) show the PML configurations in the geometrical model with single and double cylinders, respectively. The double cylinders in figure 3(*d*) are symmetric about the horizontal centerline of the computational region. Here, for comparison, we used the same computational parameters as Haydock [25].

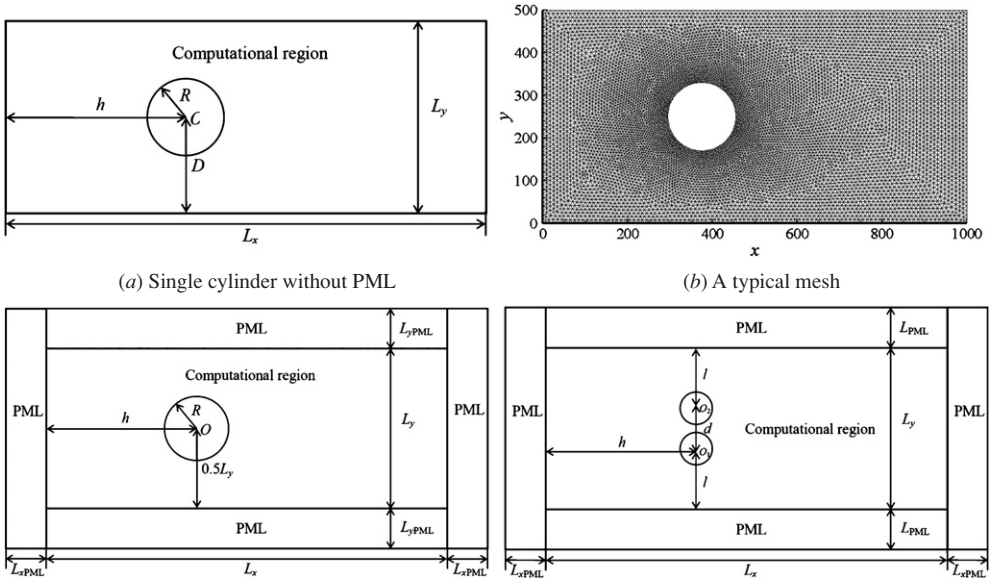


(*a*) Single cylinder without PML (*b*) A typical mesh

(*c*) Single cylinder with PMLs (*d*) Double cylinders with PMLs

**Figure 3.** Geometrical configurations.

For the model without PMLs, the left boundary is a sound source. We consider a standing wave field between the left and the right boundary. The length of the computational region is set as $L_x = \lambda$, where $\lambda$ is the wavelength. The wave is initialized as $\rho = \rho_0 + \mathrm{d}\rho\cos(kx)$ and zero fluid velocity field $\mathbf{u} = 0$, where $k$ is the wave vector, $\rho_0 = 1.0$ and $\mathrm{d}\rho = 0.01$. To generate a standing wave, the density on the left boundary is maintained at $\rho = \rho_0 + \mathrm{d}\rho\cos(\omega t)$, and the reflecting condition, $u_x = 0$, is imposed on the right boundary. The wave parameters are the wavelength $\lambda = 1000$, the sound velocity $c_0 = \frac{1}{\sqrt{3}}$, the circular frequency $\omega = 0.003\,63$ and the period $T = 1732.05$.

For the models with PMLs, the geometrical parameters of the computational region and the wave parameters are the same. However, reflections of the scattering field by the cylinder and the left and right boundaries must be avoided. Therefore, four PML regions are added outside the computational region as shown in figures 3(*c*) and (*d*). To generate a standing wave between the left and the right boundary, we set the density of the pseudo-mean flow in the left and right PMLs to be $\rho = \rho_0 + \frac{1}{2}\mathrm{d}\rho[\cos(\omega t + kx) + \cos(\omega t - kx)] = \rho_0 + \mathrm{d}\rho\cos(\omega t)\cos(kx)$ at every time step. The density of the pseudo-mean flow in bottom and top PMLs is $\rho_0$ and the velocities in all PMLs are set as $u_{mx} = 0$ and $u_{my} = 0$. The pseudo-mean flow, which sets the background flow in a PML region, is an important concept of the PML algorithm defined by Hu in [29]. The PML algorithm ensures that all perturbations and wave motions over the pseudo-mean flow will be dissipated in the PML region.

All of the physical variables are dimensionless in the calculations. As mentioned in [25], let $\mathbf{u}$, $\mathbf{x}$, $t$, $\nu$ be the dimensionless variables, where $\mathbf{u}$ is the velocity vector, $\mathbf{x}$ is the position vector, $t$ is the time, and $\nu$ is the kinematical viscosity, and $\mathbf{u}'$, $\mathbf{x}'$, $t'$, $\nu'$ are the corresponding variables in the real system. If we choose the host fluid as air ($c' = 340$ m s$^{-1}$, $\rho_0' = 1.2$ kg m$^{-3}$ and $\nu' = 1.4 \times 10^{-5}$ m$^2$ s$^{-1}$) and $\nu = 0.167$, the wavelength in the real system $\lambda' = L_x' = \lambda(\nu'/\nu)/(c'/c_0) = 1.42 \times 10^{-4}$ m and the frequency $f' = c'/\lambda' = 2.39$ MHz. If the host fluid is water ($c' = 1400$ m s$^{-1}$, $\rho_0' = 1000$ kg m$^{-3}$ and $\nu' = 1.0 \times 10^{-6}$ m$^2$ s$^{-1}$) and $\nu = 0.167$, the

**Table 1.** Acoustic radiation forces for the cases without the PML ($F_{\text{th}}$: analytical solutions presented in this paper, $F_{\text{LB}}$: calculated by the LB method, $F_{\text{COM}}$: calculated by COMSOL, $F_{\text{FVM}}$: calculated by our FVM program).

| $R$ | $L_x$ | $L_y$ | $h$ | $F_{\text{th}}$ ($10^{-5}$) | $F_{\text{LB}}$ ($10^{-5}$) | $F_{\text{COM}}$ ($10^{-5}$) | $F_{\text{FVM}}$ ($10^{-5}$) |
|---|---|---|---|---|---|---|---|
| 5 | 1000 | 100 | 375 | −1.23 | −3.04 | −1.22 | −1.25 |
| 10 | 1000 | 100 | 375 | −4.93 | −8.20 | −5.13 | −5.17 |
| 20 | 1000 | 200 | 375 | −19.65 | −25.12 | −21.13 | −21.17 |
| 40 | 1000 | 200 | 375 | −76.72 | −81.02 | −108.41 | −105.15 |
| 80 | 1000 | 500 | 375 | −257.22 | −247.20 | −384.22 | −375.30 |

wavelength in the real system $\lambda' = L_x' = \lambda(\nu'/\nu)/(c'/c_0) = 2.47 \times 10^{-5}$ m and the frequency $f' = c'/\lambda' = 56.7$ MHz.

### 5.2. *Simulations for an inviscid fluid without the PML*

We first calculate the cases with the same system conditions as Haydock [25], but zero viscosity. In this section, the PMLs are not considered, and the top and bottom boundaries of the computational region are both reflecting. Haydock used the periodic boundary conditions on the top, bottom and right boundaries, which are equivalent to the reflecting boundary conditions numerically, because the computational region is symmetric. The widths of the computational region $L_y$ with the other properties for different cases are detailed in table 1. All of the calculations are performed on a workstation with an Intel(R) Xeon(R) 5160 CPU (3.0 GHz and 4MB L2 Cache) and 8 GB RAM. It takes 7 h and 45 min for a typical case with $R = 20$ and 21 970 triangular elements.

For comparison, we also calculate all the cases by the COMSOL software, which is a commercial finite element method (FEM) software package for multiphysics problems developed by COMSOL Inc. Details of the results of the acoustic radiation force are calculated from the FVM program, COMSOL and analytical solutions [17] are given in table 1 for different particle radii.

It can be seen in table 1 that the results between our FVM program and COMSOL agree with each other well. The maximum relative difference is 3.1%, which indicates that the FVM results are correct. The differences between the two algorithms may result from the different computational meshes.

The density contours at time $100T$ computed by the FVM program are plotted in figure 4. The numerical density distortion because of the cylinder is clearly seen.

It is noted that the results from the LB method are significantly different from both the analytical solutions and the COMSOL results. The major reason is that the LB results from [25] are not in an ideal fluid but in the fluid with $\nu = 0.167$. Therefore, we believe that the LB method used by Haydock will not give an exact comparison to the analytical solution, no matter what conditions are adopted, such as lowering $\nu$. To avoid the influences of the boundary reflecting waves, we will perform the calculations with the PML in the following section.

It should also be noted that the differences between the FVM results and the analytical predictions, which are calculated from the present analytical solution by the terms up to $|m| \leqslant 4$ in equation (11), become large when the particle radius grows. We figure out that this difference comes from the reflecting boundary conditions of the surrounding boundaries of the

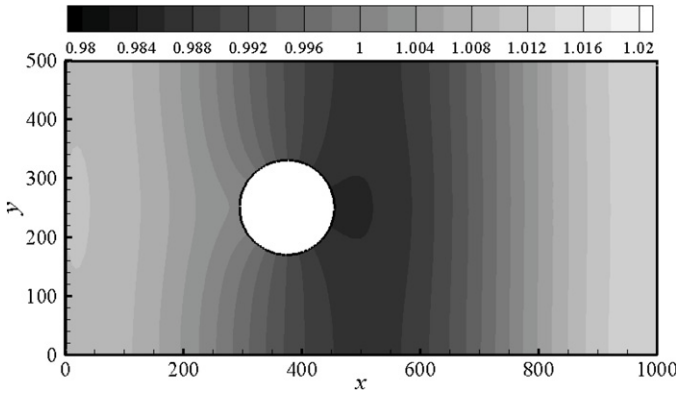


**Figure 4.** Density distribution at time 100*T*.

**Table 2.** Acoustic radiation forces for the cases with the PML ($F_{\text{th}}$: analytical solutions, $F_{\text{FVM}}$: FVM simulations).

| $R$ | $L_x$ | $L_y$ | $L_{\text{xPML}}$ | $L_{\text{yPML}}$ | $h$ | $F_{\text{th}}$ ($10^{-5}$) | $F_{\text{FVM}}$ ($10^{-5}$) | Difference ($10^{-5}$) | Difference (%) |
|---|---|---|---|---|---|---|---|---|---|
| 5 | 1000 | 50 | 50 | 50 | 375 | −1.23 | −1.24 | −0.01 | 0.813 |
| 10 | 1000 | 80 | 50 | 50 | 375 | −4.93 | −4.93 | 0.00 | 0.000 |
| 20 | 1000 | 150 | 80 | 80 | 375 | −19.65 | −19.66 | −0.01 | 0.051 |
| 40 | 1000 | 300 | 100 | 100 | 375 | −76.72 | −77.11 | −0.39 | 0.508 |
| 80 | 1000 | 500 | 100 | 100 | 375 | −257.22 | −253.18 | 4.04 | 1.571 |

computational region, because the theoretical solution only takes into account the incident and scattered waves on the particle surface and excludes the waves reflected from other surfaces.

### *5.3. Simulations for an inviscid fluid with the PML*

The widths of the computational region $L_x$ and $L_y$ as well as the PML region $L_{x\text{PML}}$ and $L_{y\text{PML}}$ with the other properties in different cases are detailed in table 2. Details of the results of the radiation force calculated from the FVM program with the PML compared with the analytical solutions are also listed in table 2 for different particle radii.

It can be seen in table 2 that the force magnitudes of the FVM results with PMLs are all less than those without PMLs. These results are now quite close to the analytical predictions. The maximum relative difference is less than 2%, which indicates that the FVM algorithm with the PML can simulate the cases in infinite space correctly and accurately.

To test the capability of the PML further, we calculate the acoustic radiation force at cylinder radius $R = 20$ with different computational region widths. Table 3 shows the computational parameters, the time-averaged forces on the cylinder and the differences compared with the analytical predictions. The percentage differences are very small in all the cases. That is to say, the PML approach works well and we have obtained the results without the influences of the top and bottom boundaries.

Table 4 lists the acoustic radiation forces of a particle with radius $R = 20$ at different positions in the computational chamber compared with the theoretical predictions. For a standing wave, the positions at $h = 250$ ($\lambda/4$), 500 ($\lambda/2$) and 750 ($3\lambda/4$) are the nodes or

**Table 3.** Acoustic radiation forces for the cases with the PML at different $L_y$, $R = 20$ ($F_{\text{th}}$: analytical solutions, $F_{\text{FVM}}$: FVM simulations).

| $L_x$ | $L_y$ | $L_{x\text{PML}}$ | $L_{y\text{PML}}$ | $h$ | $F_{\text{th}}$ ($10^{-5}$) | $F_{\text{FVM}}$ ($10^{-5}$) | Difference (%) |
|---|---|---|---|---|---|---|---|
| 1000 | 50 | 100 | 100 | 375 | −19.65 | −19.60 | 0.254 |
| 1000 | 100 | 100 | 100 | 375 | −19.65 | −19.69 | 0.204 |
| 1000 | 150 | 80 | 80 | 375 | −19.65 | −19.66 | 0.051 |
| 1000 | 200 | 80 | 80 | 375 | −19.65 | −19.66 | 0.051 |
| 1000 | 250 | 80 | 80 | 375 | −19.65 | −19.58 | 0.356 |

**Table 4.** Acoustic radiation force with the PML at different positions, $R = 20$ ($F_{\text{th}}$: theoretical solutions, $F_{\text{FVM}}$: FVM simulations).

| Position $h$ | $F_{\text{th}}$ ($10^{-5}$) | $F_{\text{FVM}}$ ($10^{-5}$) | Difference ($10^{-5}$) | Difference (%) |
|---|---|---|---|---|
| 125 | 19.65 | 19.51 | −0.14 | 0.712 |
| 250 | 0 | 0.079 | 0.079 | – |
| 375 | −19.65 | −19.66 | −0.01 | 0.051 |
| 500 | 0 | −0.017 | −0.017 | – |
| 625 | 19.65 | 19.65 | 0.0 | 0.0 |
| 750 | 0 | −0.015 | −0.015 | – |
| 875 | −19.65 | −19.49 | 0.16 | 0.814 |

anti-nodes of pressure and velocity, where the acoustic radiation force is zero. The maximum forces which can be predicted by the analytical formulations in section 2 appear at the positions between one pressure and the next velocity node where $h = 125$ ($\lambda/8$), $h = 375$ ($3\lambda/8$), 625 ($5\lambda/8$) and 875 ($7\lambda/8$). It is shown in table 4 that the numerical results agree with the theoretical solutions very well, with a maximum percentage difference is less than 1%.

### *5.4. Effects of viscosity*

In this section, the effects of viscosity of the host fluid are investigated. The acoustic boundary layer (thickness $\delta = (2\nu/\omega)^{1/2}$) appears surrounding the cylinder in a viscous fluid, in which the momentum transfer takes place as well as on the cylinder surface. Some more complex physical phenomena such as acoustic streaming, attenuation and change of the wave phase happen in the boundary layer and the host fluid. Only a part of this momentum transfer converts into the radiation pressure and the remainder into acoustic streaming [2]. On the one hand, the acoustic boundary layer will reduce the magnitude of the acoustic radiation force due to the energy absorption of the incident and scattered wave; on the other hand, the acoustic streaming will generate a drag force on the cylinder. In our simulations, all these effects can be taken into account simultaneously, because we solve the whole N–S equations directly. So, the numerical results produce the total mean force actually exerted on the cylinder.

Our FVM method has been shown to be precise in inviscid cases in the previous sections. Furthermore, to validate our FVM method in viscous cases, we compare the FVM results in a viscous fluid with COMSOL. The fluid viscosity is 0.167 and other parameters are also presented in table 5. Note that the cases in table 5 are all without the PML, because it is difficult to implement the PML algorithm into COMSOL. We can see that the forces are all greater than those with PML cases in table 6 because of the effects of top and bottom boundaries and also greater than the inviscid cases. The results between our FVM method and COMSOL

**Table 5.** Mean forces for the viscosity $\nu = 0.167$ without the PML ($F_{\mathrm{COM}}$: COMSOL simulations, $F_{\mathrm{FVM}}$: FVM simulations).

| $L_x$ | $L_y$ | $h$ | $R$ | $F_{\mathrm{LB}}$ ($10^{-5}$) | $F_{\mathrm{COM}}$ ($10^{-5}$) | $F_{\mathrm{FVM}}$ ($10^{-5}$) | Difference (%) |
|---|---|---|---|---|---|---|---|
| 1000 | 200 | 375 | 20 | −25.12 | −30.68 | −31.12 | 1.43 |
| 1000 | 200 | 375 | 40 | −81.02 | −138.83 | −141.33 | 1.80 |
| 1000 | 300 | 375 | 60 | – | −307.32 | −304.53 | 0.91 |
| 1000 | 500 | 375 | 80 | −247.2 | −444.46 | −432.21 | 2.76 |

**Table 6.** Mean forces ($\times 10^{-5}$) for viscosity versus radius at the cylinder position $h = 375$ and $L_x = 1000$ with the PML.

| $\nu$ \ $R$ | 5 | 10 | 20 | 40 | 80 |
|---|---|---|---|---|---|
| 0.0167 | −1.76 | −5.77 | −21.17 | −78.67 | −246.90 |
| 0.0835 | −2.36 | −7.12 | −23.26 | −79.64 | −232.23 |
| 0.167 | −2.75 | −8.01 | −25.00 | −81.16 | −223.73 |
| 0.333 | −3.32 | −8.96 | −27.18 | −83.02 | −214.88 |
| 0.835 | −4.36 | −10.54 | −28.69 | −85.30 | −205.30 |
| 1.670 | −4.79 | −11.51 | −26.42 | −83.26 | −192.87 |
| 3.33 | −4.47 | −10.60 | −19.76 | −67.87 | −165.20 |
| 8.35 | −3.51 | −6.08 | −7.06 | −25.40 | −95.40 |

agree with each other very well, even for large radii. The maximum relative difference is less than 2.8%, which suggests that the FVM results are correct. The LB results are also listed in table 5. Haydock [25] obtained these results at the same computational conditions as $\nu = 0.167$ without the PML. However, the LB results differ much from the results of both COMSOL and our FVM method. The exact reason is not known yet, because we cannot find any more detailed computational parameters in [25] except the geometrical and physical parameters of the fluid and the incident wave. Perhaps, the other computational conditions such as the size of a grid element and the algorithm for boundary conditions play an important role in the LB simulation.

In table 6, we present the detailed results with the PML at the cylinder position $h = 375$ for a radius from 5 to 80 with a wide viscosity range from 0.0167 to 8.35. In the viscous simulations, the non-slip boundary conditions (fluid velocity is confined to zero on the cylinder surface) are imposed on the cylinder surface. Here, we got quite different results from Haydock's [25], where the mean force in viscous cases is always greater than the inviscid prediction. We should point out that the mean force actually imposed on the cylinder is very complicated in a viscous fluid. In our numerical simulations, generally speaking, there are two different dependence profiles between the mean force and viscosity at different cylinder radii as demonstrated in figure 5. The magnitude of the mean force first increases with the increase of viscosity and then decreases after a certain viscosity in the small radius case that the radius $R$ is less than 40 (see figure 5($a$)). There is one peak on the curve of the dependence between the magnitude of the mean force and the viscosity. In the large radius case, $R = 80$ (see figure 5($b$)), the magnitude of the mean force decreases monotonically with the increase of the viscosity. We do not know the mechanism behind these dependences clearly. The valley on the profile of the case with middle radius at low viscosity may be caused by the drag force of the acoustic streaming being less than the magnitude of the force due to the viscous loss. The magnitude of the total mean force goes down finally in every case, because the drag force

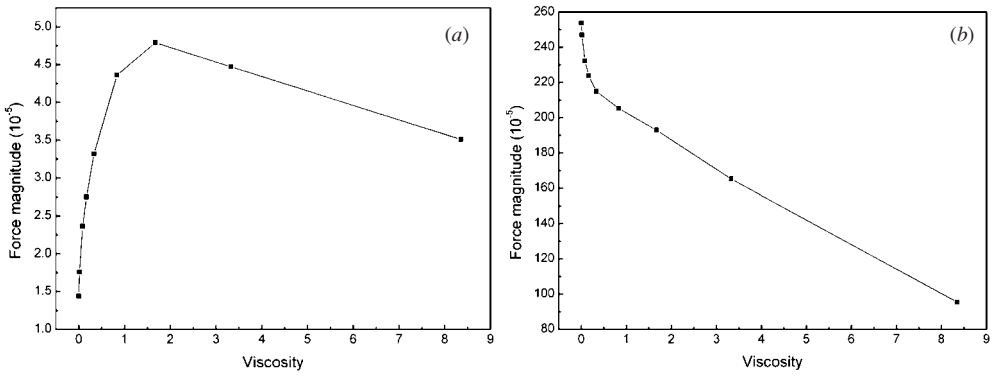


**Figure 5.** Total mean forces versus different viscosities: (*a*) $R = 5$, (*b*) $R = 80$.

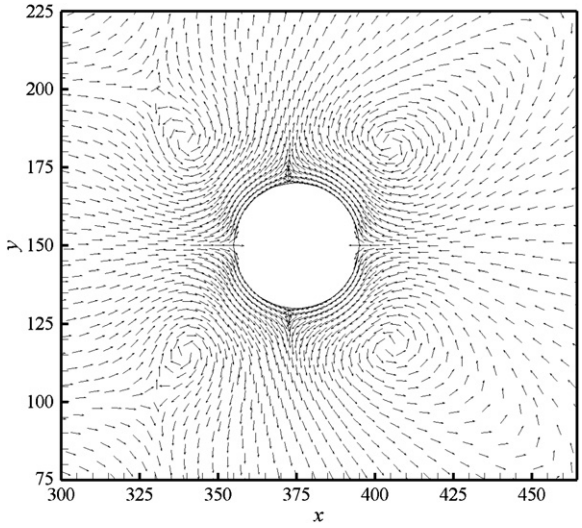


**Figure 6.** Velocity vectors of the acoustic streaming around the cylinder ($R = 20$).

of the acoustic streaming may probably change the direction with the increase of $\delta/R$. Danilov [2] discussed the viscosity effects in two limited cases that $\delta/R \ll 1$ and $\delta/R \gg 1$, but he did not mention the general dependence with arbitrary viscosity. He concluded that the drag force of acoustic streaming plays a minor role in the limit $\delta/R \ll 1$, and the drag force may be directed oppositely to the radiation pressure in the limit $\delta/R \gg 1$. This means that the total mean force may even change its sign for very large viscosities. To confirm this conclusion, the high-viscosity case with $R = 20$ and $\nu = 33.3$, where $\delta/R = 6.77$, is also calculated. The total mean force is then $4.54 \times 10^{-5}$ which is indeed directed against the radiation pressure in an inviscid fluid.

If we take the velocity field averaged over time, the time-averaged acoustic streaming field can be obtained. Figure 6 presents the velocity vectors of the acoustic streaming around the cylinder in the case $R = 20$ with viscosity 0.167. The streaming field is asymmetric

**Table 7.** Computational parameters for the secondary forces.

| $R$ | $h$ | $L_x$ | $L_y$ | $L_{\text{xPML}}$ | $L_{\text{yPML}}$ |
|---|---|---|---|---|---|
| 10 | 375 | 1000 | 150 | 50 | 50 |
| 5 | 375 | 1000 | 100 | 50 | 50 |

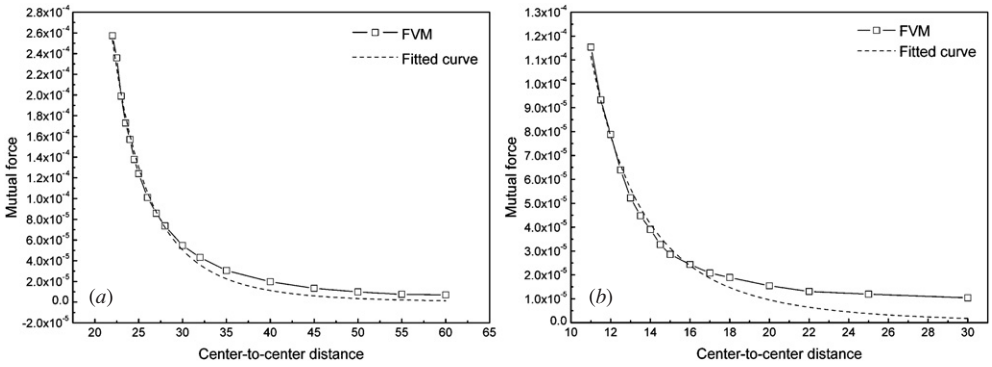


**Figure 7.** Attractive forces between two rigid cylinders in an acoustic standing wave: (*a*) $R = 10$, (*b*) $R = 5$.

about the cylinder in the horizontal direction, because the cylinder is located at the midway between a velocity node and its next anti-node. There are four outer big vortices away from the cylinder boundary as described by Nyborg [30]. Note that the stream lines are smooth close to the boundary like those in the theoretical predictions, while there are many small vortices in Haydock's LB simulations [31] which are probably caused by the boundary approximation of the LB method.

### *5.5. The secondary forces in an inviscid fluid with the PML*

As mentioned in the introduction, secondary forces will arise between two objects in a sound field. These mutual forces result from the interaction between the scattering fields of the two objects. The calculation geometry is shown in figure 3(*b*), and two cases of cylinder radius $R = 10$ and $R = 5$ are considered. The computational parameters are listed in table 7. The center-to-center distance varies from 22.5 to 60 for the case $R = 10$ and from 11.0 to 30 for the case $R = 5$.

Figures 7(*a*) and (*b*) show the time-averaged forces between two cylinders for radius $R = 10$ and $R = 5$, respectively. The simulations point out that the secondary forces in the two cases are both attractive. The dashed lines in figure 7 are the results of nonlinear curve fitting. The fitting function has the power form as $f = ad^{-b}$, where $d$ is the center-to-center distance, $f$ is the force, $a$ and $b$ are the parameters to be determined. The parameters are determined to be $a = 2461.83$, $b = 5.206$ in figure 7(*a*) and $a = 2.12$, $b = 4.109$ in figure 7(*b*), respectively. Weiser [21] gave a formula to calculate the mutual forces between rigid or compressible particles under the conditions that the acoustic wavelength is much greater than the particle radius and the center-to-center particle distance. This formula implies that the mutual force should be inversely proportional to the separating distance to the fourth

power ($d^4$). The weakening parameter $b = 5.206$, in the case $R = 10$, is close to but larger than 4.0. Moreover, when the radius decreases to $R = 5$, the parameter $b$ approaches 4.0, because the smaller radius is closer to the assumptions of Weiser's theory. At the same time, in figure 7, with the increase of the particle separation distance, the errors between the numerical results from FVM and their fitted curve with the weakening parameter close to 4.0 increase gradually, especially in figure 7($b$) with $R = 5$. This is also because of the assumptions of Weiser's theory that the separating distance should be much smaller than the wavelength.

## 6. Conclusions

In this paper, we first obtain an analytical solution for the time-averaged force on a rigid fixed cylinder in an inviscid fluid in a standing sound field, and then numerical calculations are performed with inviscid and viscous fluid using the FVM algorithm to solve the N–S equations directly. To avoid the computational region boundary reflection, the PML technique is adopted.

Our analytical solution is easy to calculate by using mathematical software packages with some truncations, and it is more common and accurate than Haydock's [17] which only takes into account terms up to the second order and is confined by the condition of small $h$.

The numerical results computed by our FVM program are compared with those of COMSOL, our analytical solution and the LB method. Good agreement with COMSOL is achieved in a closed chamber with reflecting boundaries. The PML results also agree very well with the analytical solutions. Furthermore, the effects of viscosity are investigated by the FVM program. Due to the effects of viscosity, including viscous losses and acoustic streaming drag, the mean force on the cylinder varies with the viscosity in a complicated fashion. The simulations show two kinds of complicated dependences between the mean forces acting on the cylinder and the fluid viscosity at different cylinder radii and the same conclusion as Danilov's [2] that the total mean force can change its direction at high viscosity. We also calculate the secondary forces between particles, where the results verify Weiser's law of a force inversely proportional to the distance to the fourth power.

The simulations also reveal that our numerical method based on the FVM algorithm and PML technique is quite suitable for calculating the acoustic problem. The method is shown to be correct and accurate from the comparison to the analytical prediction and COMSOL software. It can also deal with problems with complicated geometrical shapes of particles and chambers, complicated fluids and different kinds of acoustic waves. With the aid of the PML technique which is difficult to implement in most commercial software package such as COMSOL, our method is able to handle the cases in infinite and semi-infinite space. Compared to the LB method, our scheme can deal with low-viscosity fluids more conveniently, since the LB method cannot calculate inviscid cases. Moreover, the implementation of boundary conditions in our method is more accurate than the LB method, because there are no artificial small vortices close to the cylinder surface in our method as discussed in section 5.4. We believe our method has a great potential in the numerical modeling for the design of ultrasonic particle manipulation devices.

Future work should be done, to extend the model to three dimensions, introducing the solid–fluid interaction to compute the forces on compressible particles, as well as taking the effects of particle shapes into account. It is also a challenge to deal with the moving particles by the current method, where some special methods such as moving mesh and the arbitrary Lagrange–Euler method should be employed.

## Acknowledgment

The authors gratefully acknowledge the Swiss National Science Foundation (SNSF) for funding under grant no 200021-109528/1 and the helpful discussions with Professor Petros Koumoutsakos, ETH Zurich.

## References

[1] Torr G R 1984 The acoustic radiation force *Am. J. Phys.* **52** 402–8
[2] Danilov S D and Mironov M A 2000 Mean force on a small sphere in a sound field in a viscous fluid *J. Acoust. Soc. Am.* **107** 143–53
[3] Haake A *et al* 2005 Positioning, displacement, and localization of cells using ultrasonic forces *Biotechnol. Bioeng.* **92** 8–14
[4] Oberti S, Neild A and Dual J 2007 Manipulation of micrometer sized particles within a mircromachined fluidic device to form two-dimensional patterns using ultrasound *J. Acoust. Soc. Am.* **121** 778–85
[5] Laurell T, Petersson F and Nilsson A 2007 Chip integrated strategies for acoustic separation and manipulation of cells and particles *Chem. Soc. Rev.* **36** 492–506
[6] King L V 1934 On the acoustic radiation pressure on spheres *Proc. R. Soc.* A **147** 212–40
[7] Yosioka K and Kawasima Y 1955 Acoustic radiation pressure on compressible sphere *Acustica* **5** 167–73
[8] Hasegawa T and Yosioka K 1969 Acoustic radiation force on a solid elastic sphere *J. Acoust. Soc. Am.* **63** 1139–43
[9] Gor'kov L P 1962 On the forces acting on a small particle in an acoustical field in an ideal fluid *Sov. Phys.—Dokl.* **6** 773–5
[10] Westervelt P J 1951 The theory of steady forces caused by sound waves *J. Acoust. Soc. Am.* **23** 312–5
[11] Westervelt P J 1957 Acoustic radiation pressure *J. Acoust. Soc. Am.* **29** 26–9
[12] Donikov A A 1997 Acoustic radiation force on a spherical particle in a viscous heat-conducting fluid: I. General formula *J. Acoust. Soc. Am.* **101** 713–21
[13] Mitri F G and Fellah Z E A 2007 New expressions for the radiation force function of spherical targets in stationary and quasi-stationary waves *Arch. Appl. Mech.* **77** 1–9
[14] Awatani J 1955 Study on acoustic pressure (VI), radiation pressure on a cylinder *Memoirs of the Institute of Scientific and Industrial Research, Osaka University* **12** 95–102
[15] Hasegawa T *et al* 1988 Acoustic radiation force experienced by a solid cylinder in a plane progressive sound field *J. Acoust. Soc. Am.* **83** 1770–5
[16] Wu J and Du G 1990 Acoustic radiation pressure on a rigid cylinder: an analytical theory and experiments *J. Acoust. Soc. Am.* **87** 581–6
[17] Haydock D 2005 Calculation of the radiation force on a cylinder in a standing wave acoustic field *J. Phys. A: Math. Gen.* **38** 3279–85
[18] Wei W, Thiessen D B and Marston P L 2004 Acoustic radiation force on a compressible cylinder in a standing wave *J. Acoust. Soc. Am.* **116** 201–8
[19] Mitri F G and Chen S 2005 Theory of dynamic acoustic radiation force experienced by solid cylinders *Phys. Rev.* E **71** 016306
[20] Crum L A 1975 Bjerknes forces on bubbles in a stationary sound field *J. Acoust. Soc. Am.* **57** 1363–70
[21] Weiser M A H and Apfel R E 1984 Interpaticle forces on red cells in a standing wave field *Acustica* **56** 114–9
[22] Zheng X and Apfel R E 1995 Acoustic interaction forces between two fulid spheres in an acoustic field *J. Acoust. Soc. Am.* **97** 2218–26
[23] Townsend R J *et al* 2004 Modelling of particle paths passing through an ultrasonic standing wave *Ultrasonics* **42** 319–24
[24] Cosgrove J A *et al* 2004 Numerical simulation fo particle motion in an ultrasound field using the lattice Boltzmann model *Ultrasonics* **43** 21–5
[25] Haydock D 2005 Lattice Boltzmann simulations of the time-averaged forces on a cylinder in a sound field *J. Phys. A: Math. Gen.* **38** 3265–77
[26] Jameson A and Mavriplis D 1985 Finite volume solution of the two-dimensional Euler equations on a regular triangular mesh *AIAA paper* 85-0435
[27] Jameson A, Schmidt W and Turkel E 1981 Numerical solutions of the Euler equations by finite volume methods using Runge-Kutta time-stepping schemes *AIAA paper* 81-1259
[28] Deese J E and Agarwal R K 1988 Navier–Stokes cCalculations of transonic viscous flow about wing/body configurations *J. Aircr.* **25** 1106–12

[29] Hu F Q, Li X D and Lin D K 2008 Absorbing boundary conditions for nonlinear Euler and Navier-Stokes equations based on the perfectly matched layer technique *J. Comput. Phys.* **227** 4398–424

[30] Nyborg W L M 1965 Acoustic streaming *Physical Acoustic* vol IIB ed W Mason (New York: Academic) pp. 265–331

[31] Haydock D and Yeomans J M 2001 Lattice Boltzmann simulations of acoustic streaming *J. Phys. A: Math. Gen.* **34** 5201–13